

Dependence of Conductivity on the Interplay of Structure and Polymer Dynamics in a Composite Polymer Electrolyte

Robert L. Karlinsey, Lyudmila M. Bronstein, and Josef W. Zwanziger*

Department of Chemistry, Indiana University, Bloomington, Indiana 47405

Received: September 5, 2003; In Final Form: November 10, 2003

The conductivity and transport properties of a composite polymer electrolyte were studied by comparing the structure and dynamics as a function of both salt and organic–inorganic composite content. The system consisted of poly(ethylene oxide) (PEO), an organic–inorganic composite (OIC) prepared from aluminum tri-*sec*-butoxide and [(3-glycidioxy)propyl]trimethoxysilane (GLYMO) and lithium triflate (LiCF_3SO_3). The systems with and without salt yielded strikingly different physical properties when the OIC content exceeded 50%. Through analysis of ^{29}Si NMR spectra, it was found that the lithium ion of LiCF_3SO_3 (LiTf) promotes the condensation of GLYMO, which peaks near 50% OIC content. Also, short-range structural evidence for PEO–OIC blending at high OIC content was observed in the salt-free system through comparisons of the line shapes of the ^{27}Al NMR spectra. This blending is absent in the ternary system due to prominent PEO–LiTf interactions, as confirmed by X-ray, DSC, and impedance spectroscopy experiments. Furthermore, the glass transition temperature exhibits a linear increase as a function of OIC content, whereas the conductivity over this range first shows a sharp increase followed by a mild decrease. The dielectric constant also was found to vary nonlinearly with OIC content, indicating that ionic screening is modulated by OIC. Because in this system the conductivity and the glass transition temperature do not show a significant correlation, although structurally it is clear that PEO and salt are intimately mixed, a model was developed for the transport that focuses principally on the density of mobile lithium ions. The model predicts relatively constant ion mobilities and diffusion constants but a strongly varying mobile ion number density as a function of OIC content, which then explains the dependence of conductivity on OIC content in this electrolyte.

1. Introduction

Solid polymer electrolytes are of interest to replace existing liquid and paste electrode separators in secondary lithium batteries, due to advantages realized only in the solid state. For example, thin-film, solvent-free batteries eliminate leakage concerns, reduce the overall battery weight, and permit various thin-film geometries suitable for packaging or technological applications, such as power sources for the microprocessors in “smart cards”.^{1,2} In addition, electrolyte–electrode compliance is improved with polymer-based interfaces rather than those formed, for example, with solid inorganic electrolytes.³ All these features add to the appeal for developing polymer-based electrolytes with improved material properties.

The prototypical polymer electrolyte consists of a coordinating polymer (typically poly(ethylene) oxide, PEO) and an alkali salt, typically of the form LiX .⁴ Ionic conductivity is active in this system at temperatures above the glass transition, where it typically follows a Vogel–Tamann–Fulcher temperature dependence.^{5,6} The frequency dependence of the conductivity shows a marked plateau at lower frequencies.^{7,8} These observations have been explained with a dynamic bond percolation model.^{7–11} Furthermore, in most cases the conductivity is suppressed by crystalline regions. Thus, because the conductivity of the prototypical system is in fact not very high, much research has focused on optimizing it by lowering the glass transition temperature and stabilizing the resulting amorphous material

against crystallization. This general approach has yielded some successes but often at the expense of mechanical properties, and in any event has not produced materials with sufficiently high conductivity at ambient temperature.¹²

Inorganic additives of various types have been employed in attempts to improve properties of the base polymer electrolyte. In one approach, various inorganic nanoparticles have been used, including silica and alumina;^{13,14} this approach appears primarily to stabilize the amorphous phase of the polymer system but does not in general improve the transference number.¹⁵ An improvement in this latter respect comes from the use of layered inorganic materials, such as clay particles, which serve as both hosts for the polymer and the source of ions.^{16–19} The resulting materials have unity transference numbers, and markedly low activation barriers to conductivity. Finally, the inorganic material can be grafted directly to the polymer, resulting again in single-ion conductors.^{20,21}

In an attempt to combine many of the best properties of the composite systems described above, we have developed a composite electrolyte composed of PEO, a lithium salt, and an organic–inorganic composite (OIC) prepared from aluminum tri-*sec*-butoxide and [(3-glycidioxy)propyl]trimethoxysilane (GLYMO).^{22–24} This system shows marked improvement in conductivity and transference numbers over pure PEO-based polymer electrolytes, and some striking differences as well. In particular, although every indication is that in this composite the conductivity is related to polymer motion, and shows the same plateau as a function of frequency as does the prototypical system, the conductivity is not well-correlated with the glass

* Corresponding author. Current address: Department of Chemistry, Dalhousie University, Halifax, NS B3H 4J3 Canada. Email: jzwanzig@dal.ca

transition temperature: in particular, as OIC is added, the glass transition temperature increases, while at the same time the conductivity also *increases* by nearly 2 orders of magnitude.

This unusual relationship between the glass transition temperature and the conductivity, together with the fact that only one glass transition event is observed and is at a point typical of PEO-based electrolytes, suggests that in this composite there are different effects at work than either just polymer mobility, as described for example by dynamic bond percolation,^{8–11,25,26} or interfacial effects, as treated for example by an effective medium theory.^{27,28} We argue in this paper that in this composite system the number density of mobile ions is strongly affected by the OIC content, whereas the mobility follows the usual correlation with polymer mobility and hence glass transition. Our model includes the lithium–PEO interaction and also accounts for the stiffening of the polymer matrix through changes in PEO viscosity. Upon calculation of lithium ion number densities, we show the model qualitatively agrees with the observed conductivity trend.

2. Experimental Section

PEO (100 kDa), LiCF₃SO₃ (LiTf), and aluminum tri-*sec*-butoxide were obtained from Aldrich and [(3-glycidyloxy)propyl]trimethoxysilane (GLYMO) was obtained from Fluka. All materials were used without further purification. The polymer-to-salt ratio was fixed at 14:1, the optimal ratio for conductivity as determined previously,²⁴ and the organic–inorganic composite (OIC) consisted of the GLYMO and aluminum tri-*sec*-butoxide (Al(O^{*sec*}Bu)₃) in a 80:20 ratio. The shorthand used to label each solid polymer electrolyte is (PEO)₁₄LiTf + OIC. Synthesis of the solid polymer electrolyte through a sol–gel route has been described previously.²² Uniform films were obtained by spin coating the electrolyte solution onto Teflon supports. Samples were then placed in an oven for 2 h at 60 °C at 1 atm to evaporate the remaining solvent. Subsequently, the samples were then cured at 130 °C in a vacuum ($\sim 10^{-2}$ atm) to complete condensation for 1 h. The films were then extracted from the oven and immediately placed in a desiccator at room temperature. Film thicknesses between 80 and 265 μ m were obtained, as measured with a micrometer. Samples were stored in plastic vials and sealed with Parafilm. Measurements were made within a week of preparation but typically after 1 or 2 days. Thermogravimetric analysis (TGA) with mass spectrometric detection revealed that at most five percent weight loss occurred in all samples above 130 °C, and that this weight loss was decomposition products, not free water.

Density measurements were obtained using a 10 mL pycnometer. A nonpolar solvent, *n*-pentane, was used to make the measurements to prevent dissolution of the polymer composite. The vial was weighed before and after introduction of the composite using a Mettler-Toledo AE 200 balance. The mass of solvent displaced was related to the composite volume with the consideration that the two phases did not mix significantly. At least 10 measurements were made for a given electrolyte composition. High-purity aluminum (>99.99% Aldrich, 2.700 g cm⁻³) was used as a reference. The PEO volume fraction was then obtained from the density determined here and the known density of pure PEO (Aldrich, 1.13 g cm⁻³) at room temperature.

Powder diffraction patterns were collected on a Scintag Θ – Θ powder diffractometer with a Cu K α source (1.54 Å). Deconvolution of crystalline features enabled the percent crystallinity to be calculated and was estimated to be the intensity contribution of crystalline features relative to the overall intensity.

TABLE 1: Percent Crystallinity, χ_c , and Melting Enthalpies, ΔH , for Various Compositions^a

system	% χ_c	ΔH (J g ⁻¹)
PEO	94.0	177.1
(PEO) ₁₄ LiTf	78.0	97.0
(PEO) ₁₄ LiTf + 40% OIC	55.5	30.4
(PEO) ₁₄ LiTf + 47% OIC	43.5	16.7
(PEO) ₁₄ LiTf + 55% OIC	<10%	3.2
(PEO) ₁₄ LiTf + 70% OIC	<10%	1.8
OIC	amorphous	
PEO + 40% OIC	92.7	61.4
PEO + 55% OIC	86.8	42.6
PEO + 70% OIC	47.4	7.6

^a Crystalline fractions were determined from X-ray experiments, and specific enthalpies were obtained by examination of the endothermic transition of the DSC thermograms. For the ternary systems with 55 and 70% OIC, there were no pronounced Bragg peaks indicative of long-range order. Instead, the crystalline fractions are thought to arise from finite-size effects, which are estimated to be less than 10% of the overall intensity.

Solid-state ²⁷Al and ²⁹Si NMR were performed using a Bruker Avance DSX spectrometer. Spectra from both nuclei were obtained using a 4 mm magic angle spinning (MAS) probe with the spin rate locked at 10 kHz. A single, short pulse of length 0.5 μ s with a recycle time of 0.15 s was used to acquire ²⁷Al spectra. All spectra were referenced to corundum.²⁹ Due to the low sensitivity of ²⁹Si, cross polarization from protons was employed to improve the signal. The ¹H $\pi/2$ pulse length was 5.5 μ s and the CP contact time was 1000 μ s. The recycle time was 3 s. All spectra were referenced to kaolin.³⁰ Peak analysis of the silicon environments was performed by fitting Gaussians to the NMR line shapes.

Differential scanning calorimetry (DSC) was performed with a Perkin-Elmer DSC 7 calorimeter. Sample masses varied from 5 to 20 mg and were hermetically sealed in aluminum pans. Samples were scanned between –100 and +100 °C at a rate of 10 °C min⁻¹, using liquid nitrogen as the coolant. Glass transition regions were then determined using the fictive temperature method. Both indium and cyclohexane were used to reference thermal events. Melting points and associated enthalpies were analyzed by deconvolution because observed endothermic transitions were not symmetric. Three Gaussians at most were used to accurately specify the character of the transition. In Table 1, the melting points reflect the center of gravity melting, and the tabulated enthalpy is the sum of the peak-fit areas.

AC impedance spectroscopy was used to measure conductivity and dielectric constants of spun films. To obtain good electrode–electrolyte contact, gold electrodes of a known area (0.0647 cm²) were directly attached to the film by sputter coating, using a Polaron E5100 Sputter Coater. Films were then placed in a home-built temperature controlled cell for measurements. Room-temperature measurements were performed with a HP 4192A Impedance Analyzer. The admittance response of the material was collected by sweeping the frequencies from 5 Hz to 13 MHz with a 1 V signal, using the standard circuit model of a resistor and capacitor in parallel. Bulk resistances were then extrapolated by fitting a linear regression to the bulk response of the material. Both high-purity silicon and (PEO)₁₄LiTf ($\sigma \sim 10^{-7}$ S cm⁻¹) were used as reference materials for conductivity. Dielectric constants were obtained by taking the minimum in a capacitance versus frequency curve, which suggests saturation of ion response within the material. Pure PEO ($\epsilon_r \sim 5$) was used as a reference material.³¹

3. Results and Discussion

3.1. Physical Appearance. The physical appearance of the components and systems are as follows. PEO was supplied as a white powder. Pure OIC was amorphous, as determined by X-ray (Table 1), transparent, and easily ground using a mortar and pestle. The basic electrolyte, $(\text{PEO})_{14}\text{LiTf}$, was opaque, had a yellowish tint and was elastic. The opacity of the material is attributed to the high degree of crystallinity. Finally, because the molecular weight lies well above the PEO entanglement limit (3200 g mol^{-1}),³² the intertwining PEO chains lead to the observed elasticity. Both the elasticity and high degree of crystallinity made it impossible to grind the electrolyte.

The binary, salt-free systems (PEO + OIC) were too elastic and strong to be milled, regardless of OIC content. In addition, these materials retain the opacity and yellowish color.

The ternary CPE system of $(\text{PEO})_{14}\text{LiTf} + \text{OIC}$ led to the following observations. At 40% OIC content, the composite was rubbery and great difficulty was encountered in grinding it; again, this SPE had an opaque, yellowish color. With addition of 47% OIC content the electrolyte became slightly easier to grind, and when 55% OIC was incorporated the yellowish color had diminished considerably, resulting in a more translucent film. Finally, the composition containing the most OIC (70%) was transparent and easily pulverized. All films were free of water on the basis of TGA with mass spectrometric detection, even though the initial sol–gel process is catalyzed with aqueous acid.

3.2. Structure: X-ray Diffraction. X-ray diffraction experiments have been performed on both electrolytic and nonelectrolytic polymer systems to estimate the percent crystallinity from long-range order as well as to aid in understanding the interaction between the PEO, salt, and OIC. These results along with specific enthalpies obtained by DSC are summarized in Table 1. The morphology of the PEO changes significantly in the presence of LiTf, resulting in a loss of long-range order above 50% OIC. Tabulated crystallinities for the 55 and 70% OIC compositions of the ternary system represent estimates based on finite-size effects, because no long-range order was observed in the form of sharp diffraction peaks. To assess the component largely responsible for such changes, salt-free composites were also examined. Although the crystalline character becomes attenuated with added OIC, Table 1 shows that the crystalline fraction, χ_c , for the binary system persists even at high OIC content relative to the ternary system. The drop in crystallinity cannot be attributed simply to diminishing amounts of PEO as the OIC content increases, because the specific enthalpy is roughly 4 times as great in the binary system when the composition consists of 70% OIC. Instead, it is likely that the OIC blends with the PEO, thus creating a more disordered environment.^{33,34} The nature of the interplay among the constituents of the binary and ternary systems will be developed in subsequent sections by incorporating results from NMR and DSC. On the basis of these X-ray results alone, it appears that the extent of PEO–LiTf interactions is enhanced with increasing OIC content and generates significant morphological distortions as reflected in the crystalline fractions and specific enthalpies listed in Table 1.

3.3. Structure: ^{29}Si and ^{27}Al NMR. Solid-state ^{29}Si and ^{27}Al MAS NMR experiments were performed to probe the short-range order of the OIC of both the binary and ternary polymer systems. Although the OIC is also composed of carbon and hydrogen, it is difficult to distinguish between the PEO and OIC contributions to the ^{13}C and ^1H environments, and in fact, the NMR spectra of these nuclei did not contrast markedly. As

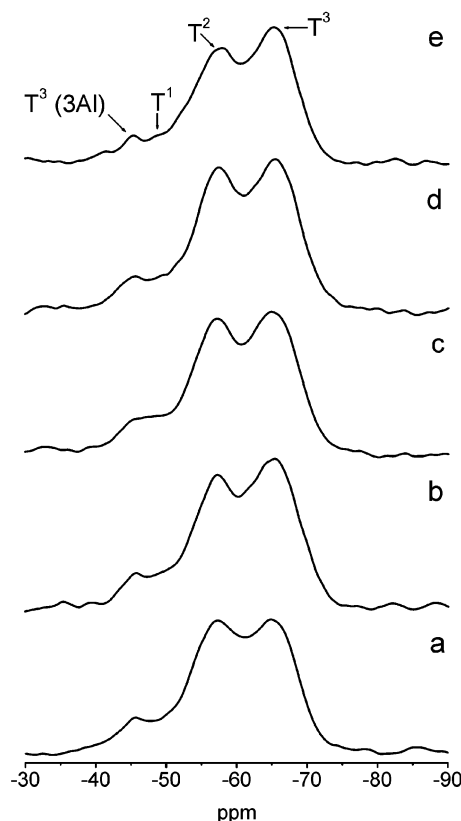


Figure 1. ^{29}Si NMR spectra of the electrolytic polymer system $(\text{PEO})_{14}\text{LiCF}_3\text{SO}_3 +$ (a) 40% OIC, (b) 47% OIC, (c) 55% OIC, (d) 70% OIC, and (e) 100% OIC.

a result, these spectra are omitted from the present discussion but can be found in previous work.²² The ^{29}Si spectra for the polymer systems are given in Figures 1 and 2, and the ^{27}Al spectra are provided in Figures 3 and 4. In addition, the spectra for the pure OIC are also shown.

With respect to silicon, there are four principal environments typical for this organically modified aluminosilicate, as indicated in Figures 1 and 2.³⁵ These so-called T^n environments denote the number of bridging oxygens comprising the network structure and can be described chemically as $\text{R-Si}-(\text{OH})_{3-n}-\text{O}_{n/2}$. On the basis of Figures 1 and 2, the downfield peak near -46 ppm has been assigned to full substitution of network aluminum in the second coordination sphere of silicon, $\text{RSi}(\text{OAl})_3$.³⁵ Next, the T^1 site is generated by incomplete condensation of the silicon moiety, with the chemical shift lying upfield, near -51 ppm . As a result, condensation of GLYMO proceeds principally in one dimension. The T^2 site, near -57 ppm , represents an increase in network development, with the condensation extended to two dimensions. In addition to the species described above, it is likely that species of the form $\text{RSi}(\text{OAl})_2\text{OSi}$ and $\text{RSi}(\text{OAl})_2\text{OH}$ also exhibit resonances that overlap those in the T^1 and T^2 sites.³⁵ Due to the broad distribution of aluminum and silicon sites that results, along with the amorphous nature of the OIC, broad NMR line shapes are expected.^{36,37} Finally, the fully condensed silicon center of GLYMO resonates farther upfield near -66 ppm due to condensation of all three functional attachments. This high degree of condensation promotes the evolution of a three-dimensional aluminosilicate network.

^{27}Al NMR has also been employed and complements the ^{29}Si characterization of the OIC. Figures 3 and 4 depict the tetrahedral and octahedral environments of aluminum lying at 49 and 0 ppm , respectively. In aluminosilicate materials,

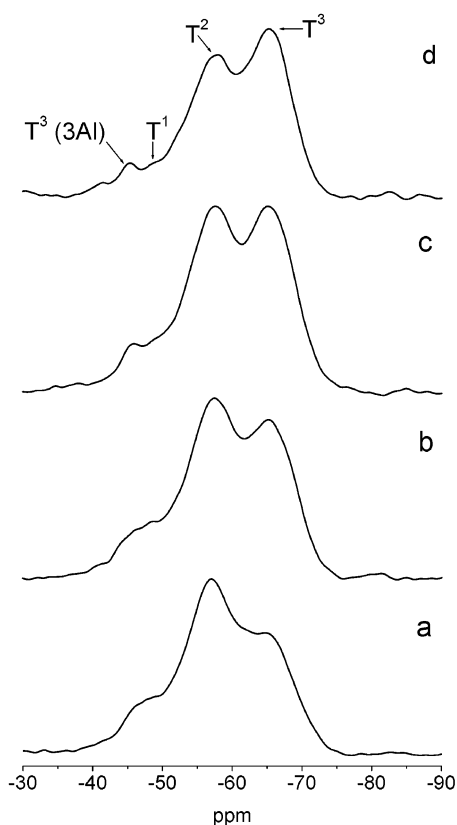


Figure 2. ^{29}Si NMR spectra of the nonelectrolytic polymer system PEO + (a) 40% OIC, (b) 55% OIC, (c) 70% OIC, and (d) 100% OIC.

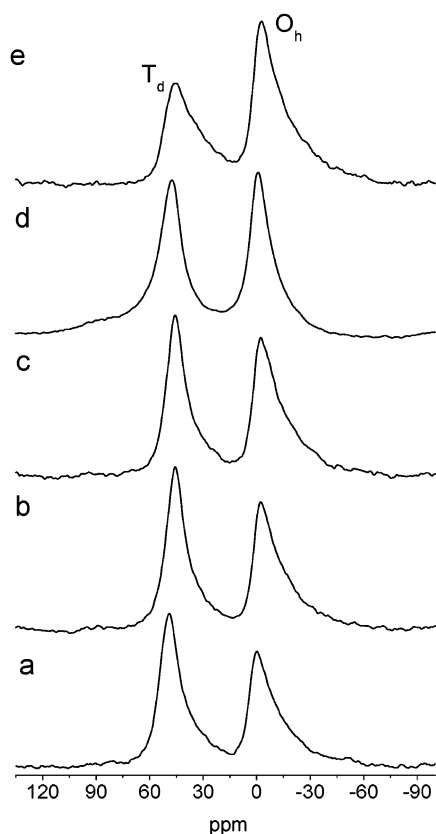


Figure 3. ^{27}Al NMR spectra of the electrolytic polymer system $(\text{PEO})_{14}\text{LiCF}_3\text{SO}_3$ + (a) 40% OIC, (b) 47% OIC, (c) 55% OIC, (d) 70% OIC, and (e) 100% OIC.

tetrahedral aluminum $[\text{AlO}_4]^-$ is considered to be network forming³⁸ and can participate in Al–O–Al or Si–O–Al

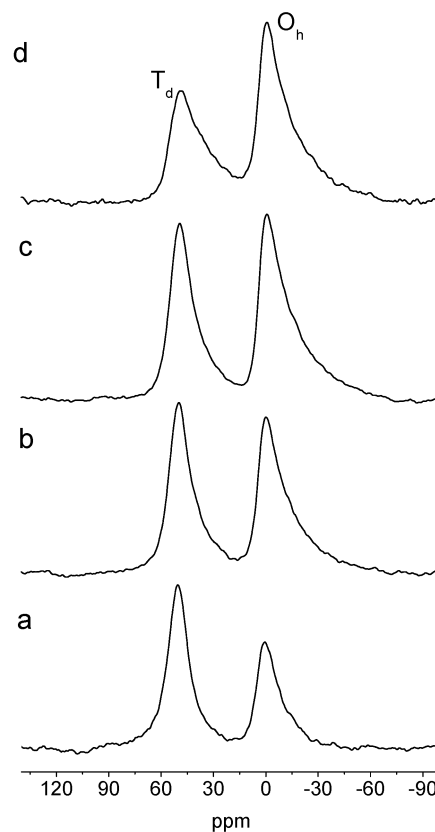


Figure 4. ^{27}Al NMR spectra of the nonelectrolytic polymer system PEO + (a) 40% OIC, (b) 55% OIC, (c) 70% OIC, and (d) 100% OIC.

TABLE 2: Intensity Percents of the ^{29}Si and ^{27}Al Environments Obtained by Deconvolution^a

system	silicon				aluminum	
	T^3 (3Al)	T^1	T^2	T^3	T_d	O_h
$(\text{PEO})_{14}\text{LiTf} + 40\% \text{ OIC}$	11	4	42	41	57	43
$(\text{PEO})_{14}\text{LiTf} + 47\% \text{ OIC}$	7	9	37	46	56	44
$(\text{PEO})_{14}\text{LiTf} + 55\% \text{ OIC}$	9	9	36	45	54	46
$(\text{PEO})_{14}\text{LiTf} + 70\% \text{ OIC}$	10	6	38	42	49	51
100% OIC	7	7	34	41	38	62
PEO + 40% OIC	9	12	43	33	61	39
PEO + 55% OIC	6	11	42	38	52	48
PEO + 70% OIC	8	11	36	40	49	51

^a Only the four pertinent sites of the T^n group are given in the table.

bonding. Also present is octahedral aluminum, which appears in various charged forms principally to aid in neutralizing the negative charge of the aluminosilicate. In addition, octahedral aluminum may participate in network formation. Due to the high reactivity of aluminum alkoxides to hydrolysis, particularly noted in sol–gel chemistry,^{39,40} aluminum oxo hydroxo complexes of the type $[\text{AlO}_x(\text{OH})_y(\text{H}_2\text{O})_z]$ are formed. In all cases, both aluminum sites are observed from NMR. Also, we note that pentacoordinate aluminum species are absent, which makes the corresponding analysis somewhat simpler. By using a short pulse length and recycle time, quantitative estimates of the populations within the T_d and O_h sites can be made.

To establish a more concrete comparison of the spectra, deconvolution of the NMR line shapes was performed. Analyses of the silicon and aluminum spectra are summarized in Table 2. The tabulated intensity percents are the result of fitting peaks to the NMR line shapes. A minimum number of Gaussians were used to accurately depict the ^{29}Si NMR line shape. Typically, five were used; however, the 100% OIC system required six Gaussians. Only the principal four peaks are shown in the table.

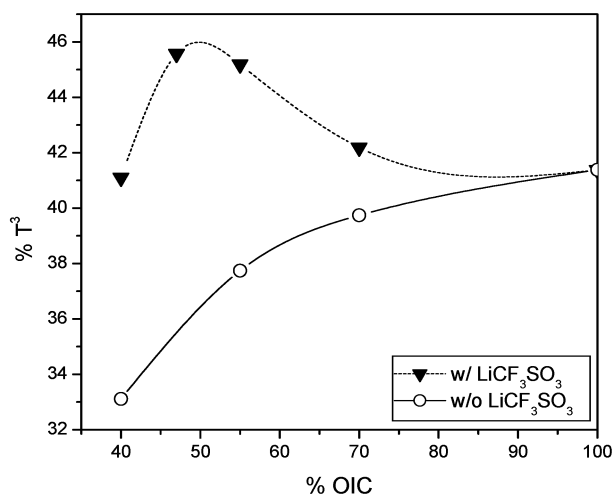


Figure 5. Development of silicon T³ character expressed as the intensity percent given in Table 3 for both electrolytic and nonelectrolytic polymer systems.

For the ²⁷Al spectra, the intensities were simply taken with no deconvolution, because fitting the octahedral site to Gaussians, for example, would be highly subjective due the variety of the aluminum oxo hydroxo species possible.

3.3.1. ²⁹Si NMR. On the basis of the tabulated intensities of silicon sites in Table 2, the salt-free system exhibits relatively large T¹ and T² populations at 40% OIC, whereas the population of the T³ site (3Si) steadily increases as the composition approaches 100% OIC. The correlation between OIC T³ development and diminishing long-range order of PEO suggest the two components remain spatially separated. As a result, there exists a PEO and OIC interface due to penetration of individual PEO molecules into the developing aluminosilica, which disrupts condensation. Similar observations have been reported for salt-free PEO–silica compositions.⁴¹ The structural changes generated through PEO–OIC interfacing are likely to be manifested also through other chemically active sites of the OIC, such as aluminum, and will be discussed below.

With the inclusion of LiTf into the PEO + OIC system, the populations of the Tⁿ sites vary in a dramatic way. The population of T³ (3Al) is slightly elevated at all compositions relative to the salt-free compositions, whereas T¹ and T² are slightly less populated, until the composition approaches 70% OIC. The major population changes in the table, however, occur in the T³ site. Increase of T³ (3Al) and T³ species fractions means improved 3-D character of the OIC. This can be explained by formation of PEO + LiTf domains and absence of individual PEO chains able to penetrate the OIC, as described in our preceding paper.⁴² To better illustrate the contrast between the two systems, the relative intensities of the fully condensed T³ site are graphed in Figure 5 as a function of OIC content. At all compositions, the T³ site is prominently favored in the ternary system and contrasts distinctly with the low populations of the same site in the salt-free system. Possible explanations for these differences are given below.

For the binary system at low OIC content, apparently the condensation of OIC is precluded due to high PEO volume fraction, which serves to isolate OIC moieties. At the same time, participation of aluminum in Si–O–Al bonding is almost independent of the PEO fraction as these sites are mainly formed before incorporation of PEO into the system: aluminum alkoxide is much more reactive than GLYMO and its fraction in OIC is only 20 mol %.

TABLE 3: Measured Properties of (PEO)₁₄LiTf + OIC Systems

% OIC	resistance (kΩ)	σ_{RT} (S cm ⁻¹)	ϵ_r	vol frac, ϕ_{PEO}	T_g (°C)	T_m (°C)
0	555.7	2.26×10^{-7}	14.7	0.820	-57.0	56.6
40	12.4	2.82×10^{-5}	30.1	0.584	-51.1	42.7
47	34.3	9.51×10^{-6}	16.4	0.446	-50.4	47.1
55	38.9	6.57×10^{-6}	16.0	0.429	-48.0	49.1
70	200	1.51×10^{-6}	9.4	0.335	-49.2	49.3

Slight variations in the fraction of T³ (3Al) sites can be due to other mixed Si–O–Al species, i.e., RSi(OAl)₂OSi and RSi(OAl)₂OH, having resonances that overlap with those corresponding to the less-condensed T¹ and T² sites. It is not surprising that these species exist, because about 60% of the aluminum is considered to be network forming, as listed in Table 2. At higher OIC content, the T³ character begins to dominate and ultimately approaches that of pure OIC. Because the silicon-to-aluminum ratio is 80:20, this improvement can be attributed to the proximity of GLYMO species that prevails, as PEO penetration into OIC is limited due to its low volume fraction.

One reason for the improved T³ and T³ (3Al) character in the ternary system may be the complexation of PEO with Li salt and formation of PEO + LiTf domains;⁴² thus the condensation of OIC is not obstructed by incorporation of PEO macromolecules. However, one would expect a linear increase of three-dimensional OIC character by this reasoning alone, which is clearly not observed in Figure 5. Another possibility that may explain the nonlinear trend in OIC dimensionality is the presence of Li⁺, which may serve as an acid catalyst in the condensation of the aluminosilicate. Because the sol–gel synthesis of these electrolytes is performed under acidic conditions with a pH between 2 and 3, it is possible that Li⁺ interacts in a similar way as the H⁺ does during condensation.⁴³

Returning to Figure 5, the highest degree of T³ character for the ternary system lies near 50% OIC. The trend between 40% and 47% OIC content shows a rather steep incline, indicating the best conditions for condensation result from high surface-to-volume ratios of OIC. Presumably, this happens when the volume fractions between OIC and PEO become comparable (Table 3). Beyond 50% OIC content, however, a gradual decline in T³ is observed. This behavior may be related to the reduced OIC surface area formed at higher OIC content.⁴² At 70% OIC, this effect is most pronounced as seen in the slightly elevated population of the less-condensed T² site. This is reasonable, because the PEO:Li ratio is constant at all compositions, implying the decrease in T³ population cannot simply be a result of reduced lithium percent in the sample.

3.3.2. ²⁷Al NMR. The relative populations of octahedral and tetrahedral aluminum are listed in Table 2 on the basis of the spectra in Figures 3 and 4. To better assess changes in aluminum environments, the fraction of octahedral aluminum is plotted in Figure 6 for the binary and ternary systems. Although the overall ratio of $O_h:T_d$ is maintained independent of the number of components present, there are subtle differences between the binary and ternary systems below 50% OIC. The O_h site is preferentially favored in the ternary systems and appears to gradually increase up to about 50% OIC, whereas a steep increase is observed in the binary system up to the same composition. Beyond 50% OIC, the trends for the two systems nearly coincide. Presumably, the degree to which lithium participates in Si species condensation catalysis is responsible for the observed behavior. Because condensation was improved not only for the T³ site but also the T³ (3Al) site (Table 2), it is reasonable that the T_d and O_h populations shift, where

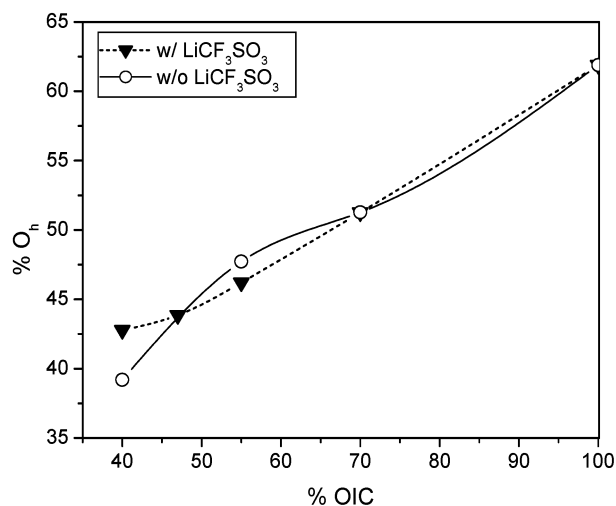


Figure 6. Intensity percent of 6-fold aluminum as a function of OIC in both electrolytic and nonelectrolytic systems.

flexibility is afforded through a large distribution of possible aluminum oxo hydroxo species. This flexibility enables aluminum to react with GLYMO residues through either the silanol groups (i.e., R–SiOH) or lithium-capped complexes (i.e., R–SiOLi) to produce Si–O–Al bonding.

The relatively high octahedral population at 40% OIC in the ternary system suggests Si–O–Al bonding arises primarily through six-coordinate network aluminum. In addition, comparisons in the line shapes of 40% OIC in Figures 3 and 4 show the broad O_h feature extends a little farther past -30 ppm in the ternary system, whereas the line shape terminates into the baseline at the same chemical shift in the binary system. As the fraction of OIC is further increased, the distribution of octahedral species will resemble that in the binary system, as evidenced in the similar widths of the line shapes in Figures 3 and 4 for 55% OIC compositions. Strangely, at 70% OIC the populations of O_h are the same for the ternary and binary systems; however, the line shapes contrast markedly: the line shape in the ternary system terminates by -30 ppm but continues past -60 ppm in the binary system. This broad distribution that extends further upfield in the binary system indicates a higher degree of shielding is present and may not be unique to species of the form $[AlO_x(OH)_y(H_2O)_z]$. From the percent crystallinity data for the binary system in Table 1, the difference in crystallinity is about 7% between 40 and 55% OIC and increases to almost 40% between 55 and 70%. Such a dramatic change in crystallinity coupled with a high degree of shielding may be explained as follows. When PEO is used for silica templating at high PEO fraction, PEO macromolecules are prone to some aggregation, causing mesopores in the templated silica.⁴¹ In addition, OIC dimensionality is rather low according to Figure 5. In our case, one might suggest that at 40 and 55% of OIC, both aggregates of PEO and low OIC volume fraction impede penetration of PEO macromolecules into OIC, which results in higher PEO crystallinity. At higher OIC content, the dimensionality and volume fraction of OIC is increased, which enables PEO to penetrate more successfully into OIC, thus increasing the opportunity for PEO–OIC coordination to develop, which would subsequently obstruct PEO crystallization. Further evidence for PEO–Al coordination through PEO penetration into OIC is provided by DSC, which is discussed in the following section. However, the absence of these features in the ternary system suggests the OIC and PEO are not interfaced in the same way as they are in the binary system.

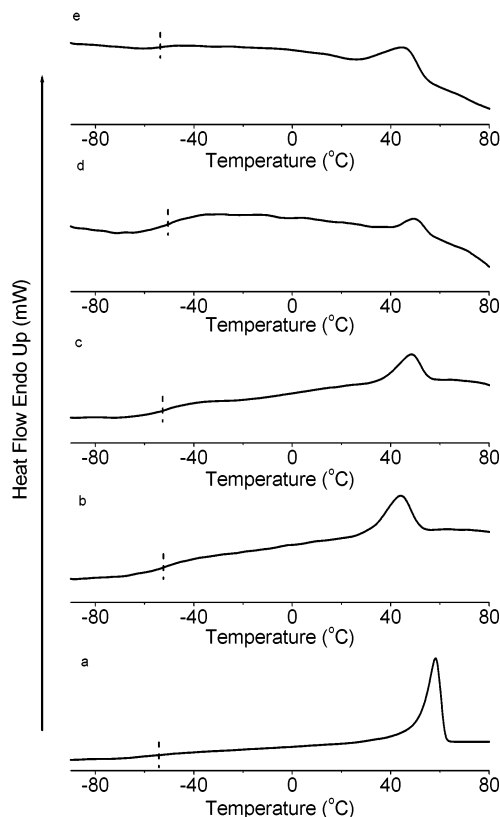


Figure 7. DSC thermograms of the nonelectrolytic polymer system PEO + (a) 0% OIC, (b) 40% OIC, (c) 47% OIC, (d) 55% OIC, and (e) 70% OIC. Dashed lines indicate glass transition temperatures.

3.4. Thermal Properties: DSC. Insight into the nature and degree of PEO–LiTf and PEO–OIC interactions are provided using differential scanning calorimetry (DSC). Figures 7 and 8 show the thermograms of the electrolytic and nonelectrolytic systems and are not normalized. The thermogram of pure OIC (not shown) did not reveal thermal features indicative of either a glass transition region or melting transition within the experimental temperature limits. At all compositions in Figure 7, the ternary systems display an endothermic transition, which we consider to be PEO melting. Because the XRD patterns did not exhibit long-range order at all compositions, it is difficult to declare with certainty the origin of melting. Contributions to this event presumably arise from the melting of PEO crystalline domains (both long-range order and finite-size effects) and to a lesser degree from amorphous regions. Also shown in Figure 7 are the glass transition (T_g) temperatures, indicated by a dashed line.

Figure 8 summarizes the thermal response from 0 to 70 °C for binary systems, as no discernible T_g was observed with the experimental heating rate of 10 °C min⁻¹. Again, the observed melting transition is probably composed of various possible PEO morphologies. Because the melting transitions in both binary and ternary systems were not symmetric, deconvolution was performed to accurately obtain the specific enthalpies and center of gravity melting. The center of gravity melting point, along with the glass transition temperatures of the ternary systems are summarized in Table 3.

3.4.1. Glass Transitions. The fact that glass transitions are not observed in the salt-free composites is attributed to the high degree of crystallinity. The development of a T_g in the ternary systems must derive from the freedom introduced when LiTf is added to the system and PEO + LiTf domains are formed. Comparison in the percent crystallinities obtained from XRD

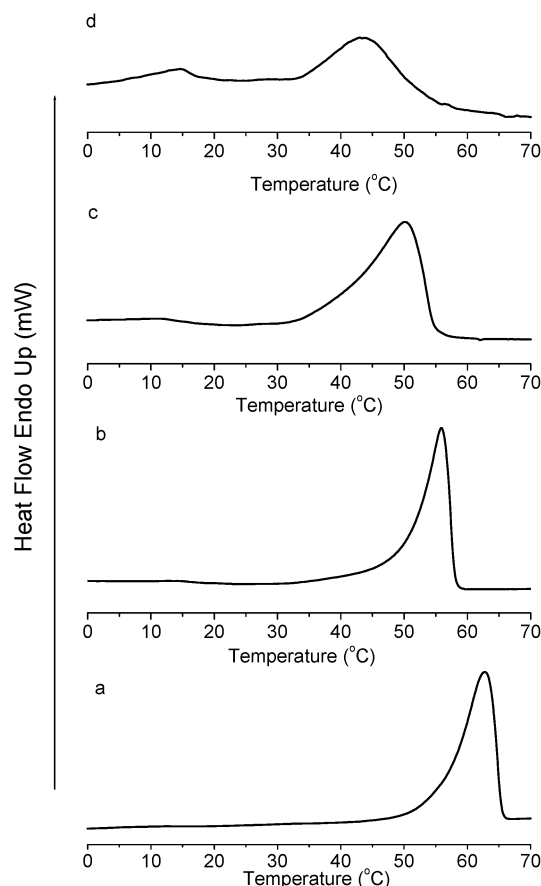


Figure 8. DSC thermograms of nonelectrolytic systems for (a) pure PEO, (b) PEO + 40% OIC, (c) PEO + 55% OIC, and (d) PEO + 70% OIC.

experiments (Table 1) of both binary and ternary systems strongly suggests that LiTf disrupts the PEO crystalline structure. This conjecture is reasonable because the formation of PEO–salt complexes is thermodynamically favorable due to the low lattice energy of LiTf relative to the solvation energy of the salt by the polymer.⁴⁴

The relationship between T_g and OIC content in Table 3 is as follows: addition of 40% OIC elevates the T_g nearly 6 deg relative to the OIC-free system, indicating PEO segmental motion has been constrained. Presumably, the elevation is due to the initial presence of the rigid OIC. However, further addition of OIC up to 70% only shifts the T_g by about 2 deg. This magnitude is small and clearly within experimental error and reveals that modulations of the PEO–OIC interface in the range 40–70% OIC do not lead to further constrained chain dynamics despite the reduced PEO volume fraction (Table 3). As a result, the OIC does not impart severe restrictions on PEO segmental relaxations in ternary systems, so the mobility of PEO is roughly the same in the OIC-free and OIC-containing electrolytic systems.

3.4.2. Melting Transitions. The melting points of the binary and ternary systems are presented in Figure 9. The distinguishing trends indicate unique behavior for the composite systems as shown in Figures 7 and 8. Several interesting features are observed in the thermograms for the binary system (Figure 8). First, we note that inclusion of 40% OIC appears to shift only the PEO melting point, with no significant changes to the endothermic profile. Indeed, this is supported by the comparable percent crystallinities obtained by XRD (Table 1). The observed depression is likely due to an increase in disorder by incorpora-

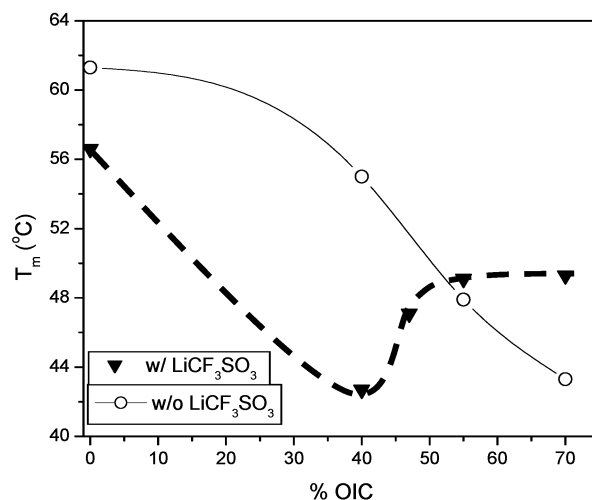


Figure 9. Melting point trends of both binary (salt-free) and ternary systems shown as a function of OIC content.

tion of amorphous OIC. At 55% OIC, again the depression is noted; however the melting profile is more distorted. Because the percent crystallinity is only reduced by 6% (Table 1), it is unlikely that disorder is introduced simply with addition of OIC. Instead, it is likely that composite-like behavior (penetration of PEO into OIC) is observed given the rather steep drop in T_m (Figure 9) and broadening of the endothermic profile. In addition, a slight endothermic wrinkle is also present near 15 °C and may hint at possible PEO–Al interactions. At 70% OIC, the profile broadens further, the percent crystallinity is dramatically reduced (drops by 40%), and the wrinkle near 15 °C becomes more pronounced. This event has also been observed in a similar system composed of PEO, LiTf, and an aluminum alkoxide (no GLYMO) and is hypothesized to be associated with octahedral aluminum complexed with PEO.⁴⁵ To ensure that the feature was not due solely to the aluminum alkoxide, DSC experiments were performed on the alkoxide itself, and no thermal event was observed at or near this point (not shown). These structural results indicate the binary system behaves strongly as a composite above 50% OIC.

The thermograms for the ternary systems in Figure 7 basically reveal the same features, including similar broadening of the melting profile at all OIC compositions. In addition, the absence of the endothermic event near 15 °C implies that O_h aluminum is shielded somewhat from PEO due to formation of PEO + LiTf domains. Due to the high reactivity of lithium and the favorable energetics of PEO–LiTf mixing, it is likely that the coordination of PEO to Li^+ is both kinetically and thermodynamically favorable relative to PEO–Al interactions. That PEO–OIC coordination is unlikely is further verified experimentally by the observation of similar T_g 's at high OIC content and also the narrow ^{27}Al O_h NMR line shape relative to that of the binary system at 70% OIC.

Though extensive mixing may not occur through PEO and OIC in the ternary system, still composite-like behavior is possible, as perceived in the melting point trend in Figure 9. The significant depression in T_m at 40% OIC is 10 deg further depressed relative to the binary system at this composition. The large difference may result from the presence of a third component, LiTf, which blends with PEO. Further addition of OIC, however, results in melting point elevation, which ultimately stabilizes at high OIC content. This behavior is not simply due to low amounts of LiTf in the system; otherwise the slopes in the ternary and binary systems would be similar

at higher OIC content. The trend appears more complicated and an explanation justifying this behavior is suggested below.

At 40% OIC, the percent crystallinity has dropped significantly, suggesting LiTf is coordinated with PEO. Also, the condensation of Si species in OIC is reasonably high, despite the low volume fraction of isolated OIC present. These aspects show there is significant mixing among the components and therefore justify the low melting temperature. However, this mixing occurs not on the molecular level (for PEO) but between OIC and PEO–LiTf domains. We note that at this composition, the material retains over 50% crystallinity and cannot be ground. These characteristics change when the OIC content is increased to 47%. At this composition the material exudes less efficient mixing, as judged by the elevated melting temperature (Figure 9). At the same time, impaired mixing means larger uninterrupted OIC domains, resulting in the highly populated T^3 sites, reduced crystallinity, and feasibility of grinding as OIC itself is brittle. The melting point continues to elevate as the crystalline fraction is further reduced. The relative order of the system is most likely changing in response to the degree of PEO–LiTf–OIC interactions at the interface. The increased OIC content results in two- and three-dimensional structures, as observed in the distribution of T^n sites in Table 2, and serves to trap PEO and LiTf at high OIC content, thereby precluding crystal growth. In effect, the material actually becomes somewhat ordered with concentrated volumes of PEO–LiTf aggregates forming at OIC content exceeding 40%.

3.5. Dielectric Constant. The dielectric constant is an important bulk parameter that should in general correlate with higher transference numbers. The relative dielectric constants for the ternary system are summarized in Table 3; note the significant maximum at 40% OIC. For reference, the dielectric constants of PEO and the pure OIC are 5 and 11, respectively.

The sharp increase in dielectric constant at 40% OIC is presumably due to the interface between PEO–LiTf and OIC, which is large, as the surface-to-volume ratio of OIC is rather high. This interface leads to the ability for lithium ions to assist in Si species condensation; with small, isolated volumes of OIC, the fraction of lithium acting as a catalyst is not rigidly constrained but is returned to the system upon condensation to contribute to system dynamics. Furthermore, we suspect that the competition between PEO and OIC for lithium leads to nonrigid PEO–Li bonds, as evidenced by the relatively low bulk resistance (Table 3) generated by mobile species. Also at this composition, the crystalline fraction is above 50%, which suggest PEO–LiTf interactions are not strong enough to preclude crystallization. The dielectric constant drops by half when the composition contains 47% OIC. At this composition, the crystalline fraction decreases below 50%. These observations indicate that the PEO–LiTf interactions successfully compete with interactions with OIC due to reduced surface-to-volume ratio, as both the 3-D character and volume fraction of OIC have increased and the bulk resistance has swelled (Table 3). At 55% OIC the dielectric constant is about the same; however, long-range order has significantly diminished according to the low crystalline fraction. Presumably, the larger volume of OIC (~60%) traps smaller PEO–LiTf domains below the critical nucleation and growth size limit. Furthermore, the volume of OIC relative to lithium increases with OIC content, so any catalytic effect of lithium is suppressed as the surface-to-volume ratio of OIC is reduced. This effect is particularly noticeable at 70% OIC, where the population of T^3 has clearly decreased relative to that of intermediate OIC content.

3.6. Conductivity. The conductivities at 293 K of the ternary systems were determined from impedance spectroscopy. The experimental spectra of these systems are shown in Figure 10. Analysis of each spectrum yields the resistance, conductivity, and relative dielectric constant. These parameters are listed in Table 3, along with the PEO volume fraction, φ_{PEO} , as determined by density measurements, and the T_g and T_m , both of which were determined from DSC. In typical solid polymer electrolytes, a decrease in the glass transition temperature is correlated with an increase in conductivity at a fixed temperature, due to the increase in polymer mobility. Table 3 shows that, in the present composites, the conductivity is not well correlated with T_g ; in fact, the conductivity increases sharply as 40% OIC is added, followed by a mild decrease at higher OIC contents, even as T_g increases. As all available evidence for the present system suggests that the T_g event is related to freezing of the polymer, and that the OIC remains static above T_g , mobility in the system above T_g must be dominated by polymer motion, just as in conventional solid polymer electrolytes. Therefore, the conductivity must be discussed in terms not just of mobility but also number density of charge carriers (predominantly Li^+).

The conductivity can be expressed as

$$\sigma = \sum_i \mu_i q_i N_i \quad (1)$$

where μ is the carrier mobility, q is the charge, and N is the carrier density of each ionic species i . All ionic species sum to yield the overall conductivity, σ . Our transference number measurements and structural data indicate that the conductivity at higher OIC content is dominated by Li^+ in these materials;²³ thus, to develop a simple approximate model of conductivity, we consider only the forces acting on a lithium ion. We model the forces as follows:

$$m \frac{dv}{dt} = -m \frac{v}{\tau} - \alpha_{\text{PEO}} v_{\text{Li}} - \frac{\varphi_{\text{Li}} z_+ q \ z_- q}{4\pi\epsilon_0\epsilon_r r^2} \left(1 + \frac{r}{\kappa}\right) e^{-r/\kappa} + z_+ q E \quad (2)$$

Here the Li^+ mass is given by m , and its velocity by v . The total force, on the left side of the equation, is set equal to the sum of the following four terms. The first is a drag term due to random ion hops from sites with residence time τ . It would dominate for high-frequency observations but is expected to be small compared to the second term, which is the viscous drag due to the fluctuating polymer. The drag coefficient α_{PEO} will be developed below. The third term is the force on the ion due to the mean field of nearby ions; this form is derived from an exponentially screened Coulomb potential. Here $z_+ q$ is the charge on Li^+ , $z_- q$ the charge on nearby counterions, ϵ_0 the permittivity of free space, ϵ_r the dielectric constant, φ_{Li} the fraction of lithium in the sample, and κ the screening length. In these relatively concentrated systems the screening length is sufficiently short that only the nearest counterions need be considered. The final term is the force due to the external electric field, which will also be considered in more detail below.

The coefficient of the viscous term is expressed as

$$\alpha_{\text{PEO}} = \varphi_{\text{PEO}} 6\pi a_{\text{Li}} \eta_{\text{PEO}} \quad (3)$$

with a representing the solvated radius of lithium (~1 Å), and η_{PEO} the viscosity. Setting the total force in eq 2 to zero in steady

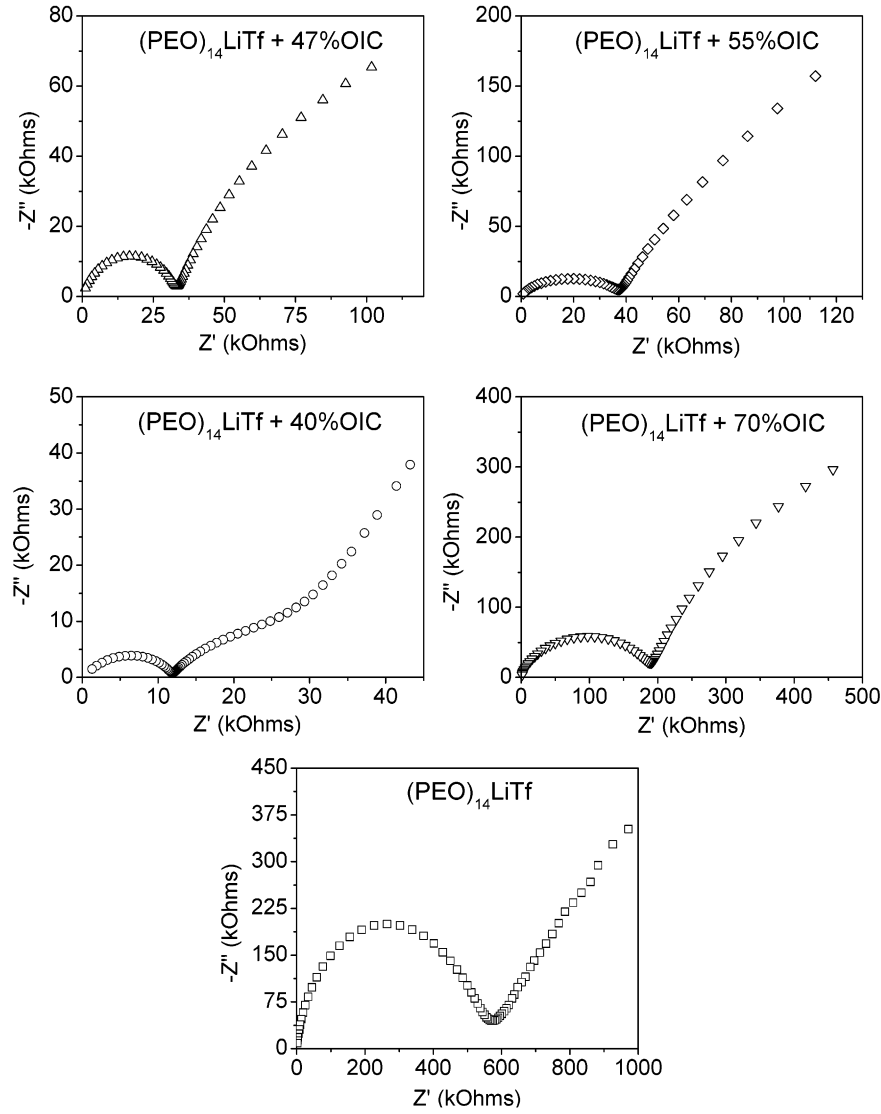


Figure 10. Impedance spectra of the electrolytic polymer systems.

state, grouping the terms including v_{Li} and substituting eq 3 into eq 2, the balance of forces becomes

$$v_{Li} \left[\frac{m}{\tau} + \varphi_{PEO} 6\pi\eta_{PEO} a_{Li} \right] = - \frac{\varphi_{Li} z_+ q z_- q}{4\pi\epsilon_0 \epsilon_r r^2} \left(1 + \frac{r}{\kappa} \right) e^{-r/\kappa} + z_+ q E \quad (4)$$

Because our model proposes that the variation in conductivity is modulated by number density, N_{Li} , we can develop v_{Li} in terms of the current density to work toward an expression for N_{Li} ,

$$J = \frac{I}{A} = z_+ q N_{Li} v_{Li} \quad (5)$$

where J is the current density, I is the current, and A is the electrode area. Substitution for v_{Li} leads to

$$\left(\frac{I}{A z_+ q N_{Li}} \right) \left[\frac{m}{\tau} + \varphi_{PEO} 6\pi\eta_{PEO} a_{Li} \right] = - \frac{\varphi_{Li} z_+ q z_- q}{4\pi\epsilon_0 \epsilon_r r^2} \left(1 + \frac{r}{\kappa} \right) e^{-r/\kappa} + z_+ q E \quad (6)$$

Finally, the electric field at the ion, E , is expressed as

$$E = E_0 + \frac{P}{3\epsilon_0} \quad (7)$$

where P is the polarization of the material and E_0 the applied external field. The surface polarization contribution is canceled in this case because the field is provided by a power supply. Computing the polarization in terms of the dielectric constant and E_0 gives

$$E = E_0 [1 + (\epsilon_r - 1)/3] \quad (8)$$

Substituting eq 8 into eq 6 and rearranging yields an expression for the number density of lithium cations participating in the conductivity:

$$N_{Li} = \frac{\left(\frac{I}{A z_+ q} \right) \left[\frac{m}{\tau} + \varphi_{PEO} 6\pi\eta_{PEO} a_{Li} \right]}{z_+ q E_0 [1 + (\epsilon_r - 1)/3] - \frac{\varphi_{Li} z_+ q z_- q}{4\pi\epsilon_0 \epsilon_r r^2} \left(1 + \frac{r}{\kappa} \right) e^{-r/\kappa}} \quad (9)$$

Using impedance spectroscopy, the external field, current,

resistance, and dielectric constant are obtained. Also, the electrode separation, h , and area, A , are known prior to experimental runs. Calorimetry provides a convenient method for obtaining glass transition temperatures, which can then be used in the Williams–Landel–Ferry (WLF) equation, which we use in the form⁴⁴

$$\log \frac{\eta_{\text{PEO}}(T)}{\eta_{\text{PEO}}(T_g)} = -17.4 \frac{T - T_g}{T - T_g + 51.6} \quad (10)$$

with $\eta_{\text{PEO}}(T_g) \approx 10^{13}$ Poise, to estimate PEO viscosity (in the absence of direct measurement). The PEO volume fraction is determined from density measurements. For the residence time τ , typical values range between 10^{-13} and 10^{-12} s.⁴⁶ We estimate the screening length from Debye–Hückel theory as

$$\kappa = \sqrt{\frac{\epsilon_r \epsilon_0 R T}{2 \rho F^2 I_{\text{salt}}}}, \quad (11)$$

with R the gas constant, ρ the polymer mass density, F the Faraday constant, and I the ionic strength of LiTf in the electrolyte (1.6 mol kg^{-1}). Because of the relatively concentrated nature of these electrolytes, the screening length provided by this model is quite short, of order 1 \AA . Because of this strong screening, the only relevant interionic distance to use in eq 9 is the nearest neighbor distance, which is of order $1/N_{\text{bulk}}^{1/3}$, where N_{bulk} is the number density of LiTf loaded into the material. Finally, the number density of ions participating in conductivity, N_{Li} , can be determined using eq 9.

Comparison between number density and conductivity is made in Figure 11. In addition, the relationship between the loading number densities and the model number densities is presented in Figure 12. The agreement in the trends between the model densities and conductivities from experiment is good, whereas the number density comparison adds strength to our assumption of strong electrolyte behavior and is consistent with results from Raman spectroscopy and NMR, which showed that the system tends toward the strong electrolyte limit as OIC is added.²³ As an additional check, we computed the lithium ion mobility from the measured conductivity and the computed number density, using eq 1, and from the mobility computed the diffusion constant. The lithium ion diffusion constant computed in this way is roughly constant as a function of OIC content, and lies between 10^{-13} and $10^{-12} \text{ m}^2 \text{ s}^{-1}$: this is in good agreement with published results.^{47,48} These supporting studies strongly support the validity of our simple approach.

Of the two resistive forces used in the model, the most sensitive appears to be the electrostatic interaction between lithium and nearby counterions, as modulated by the compositionally dependent screening constant. This term is reduced substantially at intermediate OIC content, due to the sharp rise in dielectric constant. At the same time, the viscous drag term increases, due to the increasing glass transition temperature, but not as much. The net effect is that, though the ion mobility is somewhat reduced due to the higher viscosity, more ions are free to move because of the increased screening from their surroundings.

4. Conclusion

The composite polymer electrolyte composed of lithium triflate, PEO, and an organic–inorganic composite generated from GLYMO and an aluminum alkoxide was studied as a function of both salt and OIC content. Physically, the binary

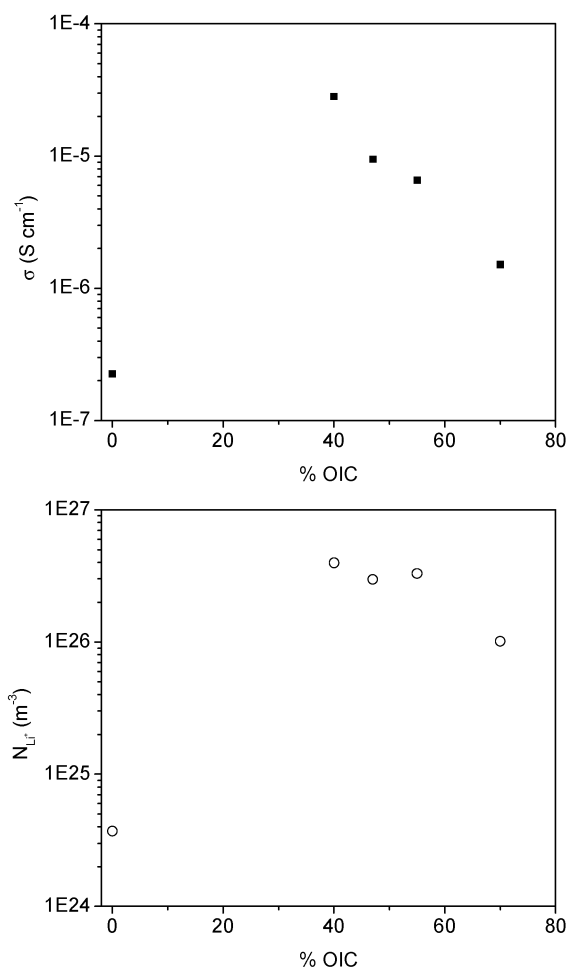


Figure 11. Trends in conductivity from experiment and calculated lithium number density from the model.

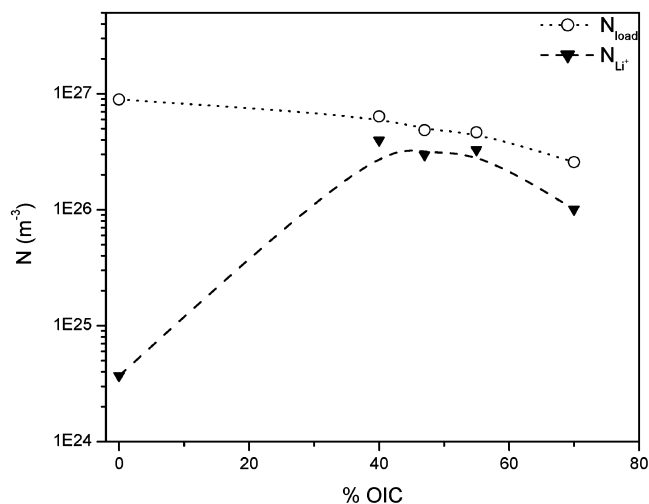


Figure 12. Comparison between loading and model-based lithium number densities.

and ternary systems yield different material properties when the OIC content exceeds 50%. Analysis of XRD patterns confirmed these observational differences with comparisons in the percent crystallinity. On the basis of analysis of ^{29}Si NMR spectra, development of 3-D structure is unimpeded at high OIC content in the salt-free system due to larger volumes of OIC and fewer penetrating PEO macromolecules. In the ternary system, however, the condensation is not linearly dependent on OIC fraction but peaks near 50% OIC. This is explained in terms of OIC

surface area and strength of PEO–LiTf interactions. Elevation of the PEO melting point hints at a more ordered environment. Also, the inability of aluminum species to interact with PEO in the presence of lithium is observed in comparison of the DSC traces of the binary and ternary systems. The lack of an additional endothermic feature throughout the ternary system compositions is ascribed to favorable PEO–Li interactions.

Given the structural evidence for pronounced PEO–Li interactions at OIC content exceeding 50%, a transport model was developed to express the number density of mobile lithium in terms of material parameters readily obtained by experiment. This model yielded ion mobilities and diffusion constants that are roughly constant with OIC content, but a density of mobile lithium ions that is a strong function of OIC content and tracks the conductivity well.

Our final conclusion from this study is that the good performance of this composite electrolyte at intermediate OIC content stems from the fact that the OIC both stiffens the material, leading to better mechanical properties, and simultaneously increases the dielectric constant, so that, rather than decreasing the conductivity due to decrease in mobility, the conductivity is increased due to an increased number of mobile lithium ions.

Acknowledgment. This work was supported with funding from a NASA grant (NAG3-2588). We thank J. C. Bollinger for assistance with powder X-ray diffraction and J. C. Carini for assistance with impedance spectroscopy. Finally, R.L.K. thanks R. A. Narayanan for invaluable discussions and support.

References and Notes

- (1) Wakihara, M. *Mater. Sci. Eng.: R* **2001**, *33*, 109.
- (2) Munshi, M. Z. A.; Owens, B. B. *IEEE Spectrum* **1989**, August, 32.
- (3) Shriver, D. F.; Bruce, P. G. *Polymer Electrolytes I: General Principles*. In *Solid State Electrochemistry*; Bruce, P. G., Ed.; Cambridge University Press: Cambridge, U.K., 1995.
- (4) Wright, P. V. *Br. Polym. J.* **1975**, *7*, 319.
- (5) Armand, M. B.; Chabagno, J. M.; Duclot, M. Poly-ethers as solid electrolytes. In *Fast Ion Transport in Solids*; Vashishta, P., Mundy, J. N., Shenoy, G. K., Eds.; Elsevier North-Holland, Inc.: Amsterdam, 1979.
- (6) Cheradame, H.; Le Nest, J. F. In *Polymer Electrolyte Reviews*; MacCallum, J. R., Vincent, C. A., Eds., 1987; Vol. 1, p 103.
- (7) Ansari, S. M.; Brodwin, M.; Stainer, M.; Druger, S. D.; Ratner, M. A.; Shriver, D. F. *Solid State Ionics* **1985**, *17*, 101.
- (8) Ratner, M. A.; Nitzan, A. *Faraday Discuss. Chem. Soc.* **1989**, *88*, 19.
- (9) Druger, S. D.; Ratner, M. A.; Nitzan, A. *Mol. Cryst. Liq. Cryst.* **1990**, *190*, 171.
- (10) Druger, S. D.; Nitzan, A.; Ratner, M. A. *J. Chem. Phys.* **1983**, *79*, 3133.
- (11) Nitzan, A.; Ratner, M. A. *J. Phys. Chem.* **1994**, *98*, 1765.
- (12) Meyer, W. H. *Adv. Mater.* **1998**, *10*, 439.
- (13) Croce, F.; Curini, R.; Martinelli, A.; Persi, F.; Scrosati, B.; Caminiti, R. *J. Phys. Chem. B* **1999**, *103*, 10632.
- (14) Croce, F.; Appetecchi, G. B.; Persi, L.; Scrosati, B. *Nature* **1998**, *394*, 456.
- (15) Johansson, P.; Ratner, M. A.; Shriver, D. F. *J. Phys. Chem. B* **2001**, *105*, 9016.
- (16) Mehrotra, V.; Giannelis, E. P. *Solid State Ionics* **1992**, *51*, 115.
- (17) Vaia, R. A.; Vasudevan, S.; Krawiec, W.; Scanlon, L. G.; Giannelis, E. P. *Adv. Mater.* **1995**, *7*, 154.
- (18) Hwang, J. J.; Liu, H. J. *Macromolecules* **2002**, *35*, 7314.
- (19) Giannelis, E. P. *Adv. Mater.* **1996**, *8*, 29.
- (20) Rawsky, G. C.; Fujinami, T.; Shriver, D. F. *Chem. Mater.* **1994**, *6*, 2280.
- (21) Fujinami, T.; Tokimune, A.; Mehta, M. A.; Shriver, D. F.; Rawsky, G. C. *Chem. Mater.* **1997**, *9*, 2236.
- (22) Bronstein, L. M.; Joo, C.; Karlinsky, R.; Ryder, A.; Zwanziger, J. W. *Chem. Mater.* **2001**, *13*, 3678.
- (23) Joo, C. G.; Bronstein, L. M.; Karlinsky, R. L.; Zwanziger, J. W. *Solid State Nucl. Magn. Reson.* **2002**, *22*, 235.
- (24) Ulrich, R.; Zwanziger, J. W.; De Paul, S. M.; Reiche, A.; Leuninger, H.; Spiess, H. W.; Wiesner, U. *Adv. Mater.* **2002**, *14*, 1134.
- (25) Druger, S. D.; Ratner, M. A.; Nitzan, A. *Solid State Ionics* **1983**, *9&10*, 1115.
- (26) Druger, S. D.; Ratner, M. A.; Nitzan, A. *Phys. Rev. B* **1985**, *31*, 3939.
- (27) Wiczorek, W.; Siekierski, M. *J. Appl. Phys.* **1994**, *76*, 2220.
- (28) Wiczorek, W.; Such, K.; Florjanczyk, Z.; Stevens, J. R. *J. Phys. Chem.* **1994**, *98*, 6840.
- (29) Woo, A. J. *Bull. Korean Chem. Soc.* **1999**, *20*, 1205.
- (30) Joao, R.; Klinowski, J. *J. Magn. Reson.* **1990**, *90*, 567.
- (31) McCrum, N. G.; Read, B. E.; Williams, G. *Anelastic and Dielectric Effects in Polymeric Solids*; Dover: New York, 1967.
- (32) Shi, J.; Vincent, C. A. *Solid State Ionics* **1993**, *60*, 11.
- (33) Templin, M.; Franck, A.; Du Chesne, A.; Leist, H.; Zhang, Y.; Ulrich, R.; Schadler, V.; Wiesner, U. *Science* **1997**, *278*, 1795.
- (34) De Paul, S. M.; Zwanziger, J. W.; Ulrich, R.; Wiesner, U.; Spiess, H. W. *J. Am. Chem. Soc.* **1999**, *121*, 5727.
- (35) Templin, M.; Wiesner, U.; Spiess, H. W. *Adv. Mater.* **1997**, *9*, 814.
- (36) Fyfe, C. A.; Gobbi, G. C.; Murphy, W. J.; Ozubko, R. S.; Slack, D. A. *J. Am. Chem. Soc.* **1984**, *106*, 4435.
- (37) Irwin, A. D.; Holmgren, J. S.; Jonas, J. J. *Mater. Sci.* **1988**, *23*, 2908.
- (38) Fyfe, C. A.; Gobbi, G. C.; Hartman, J. S.; Klinowski, J.; Thomas, J. M. *J. Phys. Chem.* **1982**, *86*, 1247.
- (39) Bradley, D. C. M.; R. C.; Gaur, D. P. *Metal Alkoxides*; Academic Press: London, 1978.
- (40) Corriu, R. J. P.; Leclercq, D. *Angew. Chem., Int. Ed. Engl.* **1996**, *35*, 1420.
- (41) Goltner, C. G.; Smarsly, B.; Berton, B.; Antonietti, M. *Chem. Mater.* **2001**, *13*, 1617.
- (42) Bronstein, L. M.; Ashcraft, E.; DeSanto, P., Jr.; Karlinsky, R. L. Jr. Zwanziger, J. W. Submitted to *J. Phys. Chem. B*.
- (43) Brinker, C. J. Jr. Scherer, G. W. *Sol–Gel Science*; Academic Press: Boston, 1990.
- (44) Bruce, P. G. Jr. Gray, F. M. *Polymer electrolytes II: Physical principles*. In *Solid State Electrochemistry*; Bruce, P. G., Ed.; Cambridge University Press: Cambridge, U.K., 1995.
- (45) Florjanczyk, Z. Jr. Zygadlo-Monikowska, E. Jr. Bzducha, W. *Electrochim. Acta* **2000**, *45*, 1203.
- (46) West, A. R. Crystalline solid electrolytes I: General considerations and the major materials. In *Solid State Electrochemistry*; Bruce, P. G., Ed.; Cambridge University Press: Cambridge, U.K., 1995.
- (47) Cheung, I. W. Jr. Chin, K. B. Jr. Greene, E. R. Jr. Smart, M. C. Jr. Abbrent, S. Jr. Greenbaum, S. G. Jr. Prakash, G. K. S. Jr. Surampudi, S. *Electrochim. Acta* **2003**, *48*, 2149.
- (48) Shin, J. H. Jr. Kim, K. W. Jr. Ahn, H. J. Jr. Ahn, J. H. *Mater. Sci. Eng.: B* **2002**, *95*, 148.